Available online at www.sciencedirect.com

ScienceDirect

Physics Procedia 61 (2015) 345 – 354

Physics Procedia

13th International Conference on Topics in Astroparticle and Underground Physics

# Solar Neutrino Results from Super-Kamiokande

Andrew Renshaw, for the Super-Kamiokande Collaboration

*Department of Physics and Astronomy, University of California, Irvine*
*3117 Frederick Reines Hall, Irvine, California 92697, USA*

**Abstract**

Super-Kamiokande-IV (SK-IV) data taking began in September of 2008, after upgrading the electronics and data acquisition system. Due to these upgrades and improvements to water system dynamics, calibration and analysis techniques, a solar neutrino signal could be extracted at recoil electron kinetic energies as low as 3.5 MeV. When the SK-IV data is combined with the previous three SK phases, the SK extracted solar neutrino flux is found to be $[2.37 \pm 0.015(\text{stat.}) \pm 0.04(\text{syst.})] \times 10^6/(\text{cm}^2\text{sec})$. The combination of the SK recoil electron energy spectra slightly favors distortions due to a changing electron flavor content. Such distortions are predicted when assuming standard solar neutrino oscillation solutions. An extended maximum likelihood fit to the amplitude of the expected solar zenith angle variation of the neutrino-electron elastic scattering rate results in a day-night asymmetry of $[-3.2 \pm 1.1(\text{stat.}) \pm 0.5(\text{syst.})]\%$. A solar neutrino global oscillation analysis including all current solar neutrino data, as well as KamLAND reactor antineutrino data, measures the solar mixing angle as $\sin^2\theta_{12} = 0.305 \pm 0.013$, the solar neutrino mass squared splitting as $\Delta m^2_{21} = 7.49^{+0.19}_{-0.17} \times 10^{-5}\text{eV}^2$ and $\sin^2\theta_{13} = 0.026^{+0.017}_{-0.012}$.

*Keywords:* Solar neutrino, Neutrino oscillation, Matter effects.
*PACS:* 14.60.Pq, 26.65.+t, 96.50.sf

## 1. Introduction

Solar neutrino flux measurements from the Super-Kamiokande (SK) [1] and the Sudbury Neutrino Observatory (SNO) [2] experiments provided direct evidence that the deficit of solar neutrinos observed by the Homestake [3] and other solar neutrino experiments is the result of solar neutrino flavor conversion. While this solar neutrino flavor conversion is well described by neutrino oscillations (in particular oscillation parameters extracted using solar neutrinos agree with those extracted using reactor antineutrinos [4]), there is still no direct evidence for this to be so. It is possible that the flavor conversion is driven by some other mechanism. However, based on the current model and parameters of solar neutrino oscillations, there are two testable signatures available for the SK experiment to look for. The first is the observation and precision measurement of the expected Mikheyev-Smirnov-Wolfenstain (MSW) [5] resonance curve. Based on the current best-fit oscillation parameters extracted using both solar neutrino and reactor antineutrino data, there is an expected characteristic energy dependence of the flavor conversion. Higher energy solar neutrinos, such as $^8$B and *hep* neutrinos, undergo complete resonant conversion within the Sun, while lower energy solar neutrino, such as *pp*, $^7$Be, *pep*, CNO and the lowest energy $^8$B neutrinos, only suffer from vacuum oscillations. After averaging the vacuum oscillations due to energy resolution, the survival probability for low energy electron

*Email address:* arenshaw@uci.edu (Andrew Renshaw, for the Super-Kamiokande Collaboration)


Selection and peer review is the responsibility of the Conference lead organizers, Frank Avignone, University of South Carolina, and Wick Haxton, University of California, Berkeley, and Lawrence Berkeley Laboratory
doi:10.1016/j.phpro.2014.12.074

flavor solar neutrinos must exceed 50%, while the resonant conversion of the higher energy solar neutrinos within the Sun leads to the currently observed survival probability of about 30%. The transition between the vacuum dominated and solar resonance dominated oscillations should occur near three MeV, making $^8$B solar neutrinos the best choice when searching for the transition point within the energy spectrum.

The second solar neutrino oscillation signature comes from the effect of the terrestrial matter density. This effect can be tested directly by comparing the rate of solar neutrino interactions during the daytime to the rate during the nighttime, when the solar neutrinos have passed through the Earth. After being resonantly converted into the second mass eigenstate within the Sun, the neutrinos which then pass through the Earth will generally have an enhanced electron neutrino flavor content. This will lead to an excess in the electron elastic scattering rate during the nighttime, and hence a negative "day-night asymmetry" $A_{\mathrm{DN}} = (r_{\mathrm{D}} - r_{\mathrm{N}})/r_{\mathrm{ave}}$, where $r_{\mathrm{D}}$ ($r_{\mathrm{N}}$) is the average daytime (nighttime) rate and $r_{\mathrm{ave}} = \frac{1}{2}(r_{\mathrm{D}} + r_{\mathrm{N}})$ is the average rate. SK observes a wide range of $^8$B solar neutrinos, making it a prime detector to search for both of the solar neutrino oscillation signatures.

The most recent solar neutrino results from the SK experiment have been presented. This includes the latest flux measurement from the fourth phase of SK (SK-IV), energy spectrum and day-night asymmetry analyses using all SK data and oscillation analyses using SK data only and then SK data plus all other relevant data (other solar neutrino and reactor anti-neutrino data). Complete details of these analyses can be found in [6, 7].

## 2. Super-Kamiokande IV Improvements

Super-Kamiokande is a 40 m diameter, 40 m tall right cylindrical stainless steel tank filled with 50 kton of ultra-pure water, located in Kamioka, Japan. The detector is optically separated into 2 distinct volumes, a 32 kton inner detector (ID) and a 2 m active veto outer detector (OD) surrounding the ID. The structure used to divide the two volumes houses an array of 11,129 50 cm photo-multiplier tubes (PMTs) facing the ID and 1,885 20 cm PMTs facing the OD. The detector itself is currently in the same configuration as during the SK-III phase [8], however improvements to the data acquisition system (DAQ) marked the end of SK-III and the beginning of SK-IV.

SK-IV began data taking in September of 2008, after having all of its front-end electronics upgraded. The new boards, called QBEEs (QTC Based Electronics with Ethernet Readout) [9], allowed for the development of a new online DAQ. The essential components of the QBEEs, used for the analog signal processing and digitization, are the QTC (high-speed Charge-to-Time Converter) ASICs, which achieve very high speed signal processing and allow the readout of every hit of every PMT. The resulting hit PMT information is sent to online computers which scan the data and use a software trigger to select time coincidences within 200 nsec, in order to pick out events. The software trigger ensures that a high rate of super low energy events does not impact the efficiency of triggering on high energy events and allows for flexible event time windows. The energy threshold using this software trigger is only limited by the speed of the online computers, and is set at 3.5 MeV recoil electron kinetic energy, the lowest of all SK phases. The triggering efficiency of SK-IV events is better than 99% at 4.0 MeV and $\sim$ 84% between 3.5 and 4.0 MeV.

Because of the large size of SK, it is necessary to continuously recirculate the water to maintain optimal water clarity. This is done by extracting water from the top of the detector, sending it through a water purification system and then re-injecting it into the bottom of the detector. If the temperature of the water being injected into the bottom of the tank is not closely matched to that of the rest of the detector, convection will occur within the tank. This allows radioactive radon (Rn) gas, which is most commonly produced near the edge of the detector by decays from the U/Th chain, to make its way into the central region of the detector. Radioactivity coming from the decay products of $^{222}$Rn, most commonly $^{214}$Bi, can mimic the recoil electron signal coming from the elastic scattering of a solar neutrino. In January of 2010, a new automated temperature control system was installed to control the temperature of the water being injected into the detector at the $\pm$0.01 K level. By controlling the supply water temperature and the rate at which water is extracted and injected to different places in the detector, convection within the tank has been kept to a minimum and the background level in the central region has become significantly lower, compared to SK-III.

Besides the above hardware improvements to the detector, a new analysis method was introduced to separate background and signal events. Even at the low energies of solar neutrinos, it is still possible to use the PMT hit patterns to reconstruct the amount of multiple Coulomb scattering a recoil electron will incur. As the energy of the recoil electron is decreased, the amount of multiple scattering the electron will incur increases, thus leading to a more isotropic PMT hit pattern. The majority of the low energy background in SK is believed to be coming from the $\beta$-decay

of $^{214}$Bi, which has an endpoint kinetic energy of $\sim$ 2.8 MeV. With the low energy threshold of SK-IV set at 3.5 MeV, the only way these lower energy $\beta$-decays contaminate the solar neutrino data set is due to Poisson fluctuations of the number of reconstructed photons, resulting in a larger reconstructed energy. However, despite these events fluctuating up in energy, they should still multiple scatter as electrons with kinetic energy less than 2.8 MeV. These $\beta$-decays should therefore undergo more multiple scattering than the solar neutrino interactions. SK-IV has introduced a new multiple Coulomb scattering goodness (MSG) variable, described in detail in [6], allowing data events to be broken into sub-samples based on the amount of multiple scattering, before the solar neutrino signal is extracted.

## 3. Detector Performance

The methods used for the vertex, direction and energy reconstructions are the same as those used for SK-III [8]. There is a very slight improvement in the vertex resolution during the SK-IV phase ($\sim$ 50 cm at 9.5 MeV), compared to SK-III, the result of improved timing resolution and timing residual agreement between data and MC simulated events coming from the upgraded front-end electronics. The angular and energy resolutions are nearly identical to the SK-III phase, $\sim 25^\circ$ and $\sim$ 14% for 9.5 MeV electrons, respectively. The absolute energy scale is determined with a small electron linear accelerator (LINAC), which injects single monoenergetic electrons into the SK tank, in the downward direction, with energies between 4.2 and 18.5 MeV. More details are described in [11]. The energy of the LINAC electrons are precisely measured by a germanium (Ge) detector. The directional and position dependence of the energy scale is further check using a deuterium-tritium (DT) fusion neutron generator [12]. The total error on the absolute energy scale resulting from these calibrations is found to be 0.54%, similar to the SK-III value of 0.53%.

The water transparency (WT) in the MC simulation is defined using absorption and scattering coefficients as a function of wavelength (see [10] for details). The dominant contribution to the variation of the WT is a variation in the absorption length. The scattering coefficients are taken as constants, while the absorption coefficient is both time and position dependent. The time variation of the absorption coefficient is checked using the light attenuation of Cherenkov light from decay electrons, resulting from cosmic-ray $\mu$'s. The position dependence of the absorption coefficient arises from draining water from the top of the detector and re-injecting it into the bottom as it is continuously recirculated. Due to the precise control of the input water temperature, the convection inside the tank is minimized everywhere but the bottom, below $z = -11$ m. Due to a small amount of convection in the bottom of the tank and a constant rising temperature above, the absorption coefficient is modeled as a constant below $z = -11$ m and with a linear function above this height. This "top-bottom" asymmetry of the WT is determined by studying the distribution of hits coming from a Ni-Cf gamma-ray source (see [10]) in the "top", "bottom" and "barrel" regions of the detector. It is found that the hit rate of the top region of the detector is 3 $\sim$ 5% lower than that of the bottom region. The time dependence of this top-bottom asymmetry is monitored using the same Ni calibration, as well as an auto-xenon calibration [10]. The introduction of this time dependent absorption coefficient has much reduced the systematic uncertainty resulting from the directional dependence of the energy scale, especially useful for the solar neutrino day-night asymmetry analysis.

## 4. Data Reduction

The majority of the analysis cuts are the same as used for the SK-III phase [8], however, in order to optimize the significance ($S/\sqrt{BG}$), the applied energy regions have slightly changed and a new tight fiducial volume cut is applied. Events between 4.5 and 5.0 MeV are cut if the radius squared $r^2$ is larger than 180 m$^2$ or the height $z$ is less than -7.5 m. Below 4.5 MeV, events are cut if they do not satisfy

$$\frac{r^2}{\mathrm{m}} + \frac{150}{11.75^4} \times \left| \frac{z}{\mathrm{m}} - 4.25 \right|^4 \leq 150, \tag{1}$$

with the coordinates given in meters. The remaining efficiency above 6.0 MeV is almost identical to SK-III, while for 5.0 to 6.0 MeV, SK-IV is better than SK-III. This is caused by removing the second vertex cut and making a looser ambient event cut. Using the new tight fiducial volume cut and a tighter ambient event cut for 3.5 to 5.0 MeV gives a lower selection efficiency, however, in exchange the background level has been much reduced.

## 5. Data Analysis

### 5.1. Total Flux

The start of SK-IV physics data taking occurred on October 6th, 2008. The results presented include data through the end of December 31st, 2012, a total of 1306.3 live days. As opposed to SK-III, which had different livetimes for the different low energy threshold periods, SK-IV took all data with the same low energy threshold of 3.5 MeV recoil electron kinetic energy. SK observes all flavors of solar neutrinos through the process of neutrino-electron elastic scattering, however, the total cross section for electron flavor neutrinos is roughly six times larger than that of the muon or tau neutrinos. This comes from the inclusion of both the charged-current (CC) and neutral-current (NC) interactions for electron flavor neutrinos, whereas the muon and tau flavors interact via the NC interaction only, making SK most sensitive the electron flavor solar neutrinos.

The differential cross section for this interaction, at the energies of solar neutrinos, is strongly peaked in the direction of the incoming neutrino. If $\theta_{\rm sun}$ is the angle between the incoming solar neutrino (which is the directional vector from the Sun to the event vertex) and the reconstructed recoil electron direction, the solar neutrino signal should peak at $\cos\theta_{\rm sun} = 1$, while background events will be mostly uniformly distributed. SK utilizes this by using an extended maximum likelihood fit between 3.5 and 19.5 MeV recoil electron kinetic energy to extract the solar neutrino flux. The same method is used for SK-I [1], SK-II [13] and SK-III [8]. The left panel of Fig. 1 shows the $\cos\theta_{\rm sun}$ distribution of the SK-IV final data sample (black points), along with the best-fit of the background (blue) and background plus solar neutrino signal (red).

The systematic uncertainties on the total flux for SK-IV were calculated using the same methods as for SK-III [8] (see [6] for full systematic uncertainty details). The total systematic uncertainty of the SK-IV flux was found to be 1.7%, improved from the 2.2% seen in SK-III, and the best value among all phases. The main contributions to the reduction come from improvements in the uncertainties arising from the energy-bin uncorrelated uncertainties; the vertex shift, trigger efficiency and the angular resolution. There is also a reduction in the uncertainties associated with the energy scale and resolution, coming from the addition of the two lowest energy bin, 3.5-4.5 MeV, for the entire period of SK-IV, compared to SK-III which use a low energy threshold of 6.0 MeV for the first half of the phase, and 4.5 MeV for the second half. The installation of the new front-end electronics has lead to a slightly better timing resolution and agreement of the timing residuals between data and MC simulated events. The total number of solar neutrino events extracted via the extended maximum likelihood fit for the SK-IV phase is $25,253^{+252}_{-250}$(stat.)±455(syst.). This number corresponds to a $^8$B solar neutrino flux of

$$\Phi_{^8\rm B}(\text{SK-IV}) = [2.36 \pm 0.02(\text{stat.}) \pm 0.04(\text{syst.})] \times 10^6/(\text{cm}^2\text{sec}),$$

assuming a pure $\nu_e$ flavor content. As seen in Table 1, the flux measurements from each phase of SK agree within the statistical errors. These four measurements can be combine together to give the total SK-I-IV combine flux of

$$\Phi_{^8\rm B}(\text{SK}) = [2.37 \pm 0.015(\text{stat.}) \pm 0.04(\text{syst.})] \times 10^6/(\text{cm}^2\text{sec}).$$

Table 1: SK measured solar neutrino flux by phase.

| | Energy Threshold | Flux ($\times 10^6/(\text{cm}^2\text{sec})$) |
|---|---|---|
| SK-I | 4.5 MeV | $2.38 \pm 0.02 \pm 0.08$ |
| SK-II | 6.5 MeV | $2.41 \pm 0.05^{+0.16}_{-0.15}$ |
| SK-III | 4.5 MeV | $2.40 \pm 0.04 \pm 0.05$ |
| SK-IV | 3.5 MeV | $2.36 \pm 0.02 \pm 0.04$ |
| Combined | | $2.37 \pm 0.02 \pm 0.04$ |

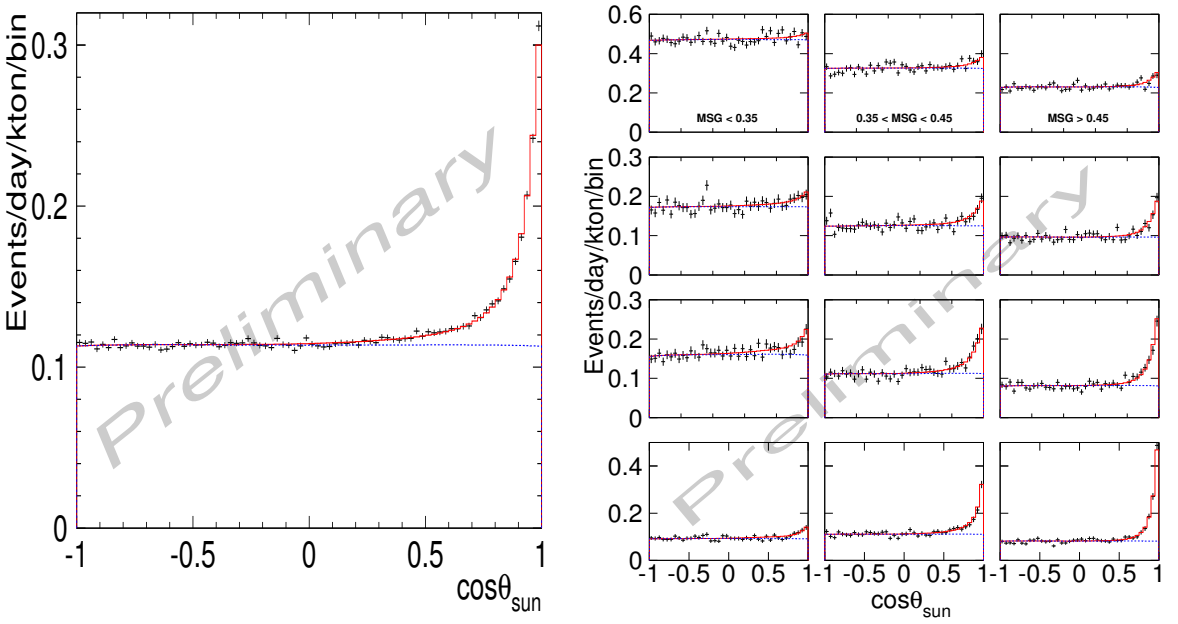


Figure 1: Left: SK-IV solar angle distribution for 3.5 to 19.5 MeV. $\theta_{\rm sun}$ is the angle between the incoming neutrino direction and the reconstructed recoil electron direction. Black points are data while the blue and red histograms are best fits to the background and signal plus background, respectively. Right: Distribution of $\cos\theta_{\rm sun}$ for the energy ranges 3.5-4.0 MeV, 4.0-4.5 MeV, 4.5-5.0 MeV and 7.0-7.5 MeV (from top to bottom), for each MSG bin (left to right). The colors are the same as the left panel.

### 5.2. Solar Neutrino Energy Spectrum

Solar neutrino flavor oscillations above about 5.0 MeV are dominated by the solar MSW [5] resonance, while low energy solar neutrino flavor changes are dominated by vacuum oscillations. Since the MSW effect rests solely on standard weak interactions, it is rather interesting to confront the expected resonance curve with data. Unfortunately multiple Coulomb scattering prevents the kinematic reconstruction of the neutrino energy in neutrino-electron elastic scattering interactions. However, the energy of the recoiling electron still provides a lower limit to the neutrino's energy. Thus, the neutrino spectrum is inferred statistically from the recoil electron spectrum. Moreover, the differential cross section of $\nu_{\mu,\tau}$'s is not just a factor of about six smaller than the one for $\nu_e$'s, but also has a softer energy dependence. In this way, the observed recoil electron spectrum shape depends both on the flavor composition and the energy-dependence of the composition of the solar neutrinos. So even a flat composition of 33% $\nu_e$ and 67% $\nu_{\mu,\tau}$ still distorts the recoil electron spectrum compared to one with 100% $\nu_e$. The energy dependence of the day-night effect and rare *hep* neutrino interactions (with a higher endpoint than $^8$B $\nu$'s) also distort the spectrum. To analyze the spectrum, we simultaneously fit the SK-I, II, III and IV spectra to their predictions, while varying the $^8$B and *hep* neutrino fluxes within uncertainties. The $^8$B flux is constrained to $[5.25 \pm 0.20] \times 10^6$ /(cm$^2$sec) and the *hep* flux to $[2.3 \pm 2.3] \times 10^4$ /(cm$^2$sec) (motivated by SNO's measurements [14, 15]).

#### 5.2.1. SK-IV Energy Spectrum

The SK-IV $^8$B solar neutrino energy spectrum is extracted using the same method as the total flux, extracting the number of signal events in 23 energy bins separately. There are 20 0.5 MeV bins between 3.5 and 13.5 MeV, two 1.0 MeV bins between 13.5 and 15.5 and one 4.0 MeV energy bin between 15.5 and 19.5 MeV. Below 7.5 MeV each energy bin is split into three sub-samples based on MSG, with the boundaries set at MSG=0.35 and 0.45. The three sub-samples in each of these low energy bins are simultaneously fit to a single signal and three independent

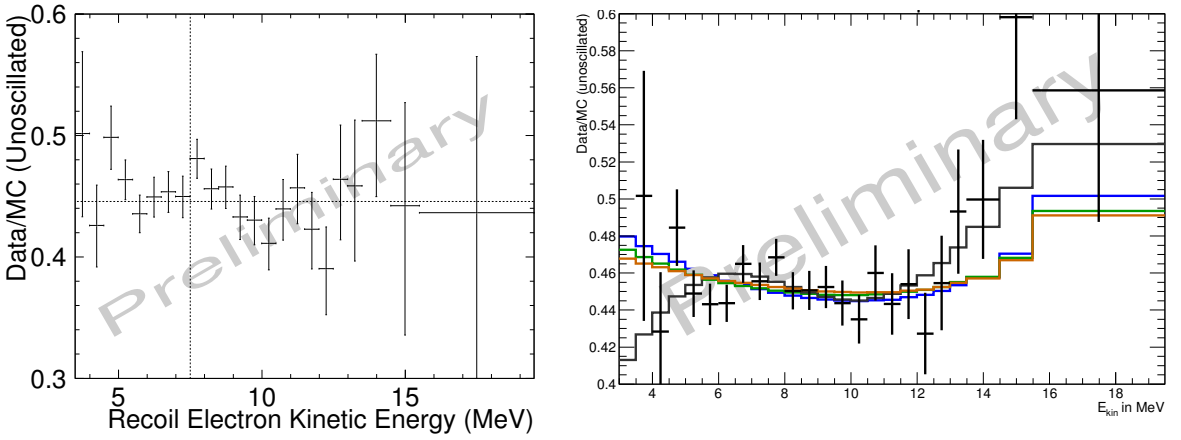


Figure 2: Left: SK-IV energy spectrum using MSG sub-samples below 7.5 MeV, shown as the ratio of the measured rate to the MC simulated unoscillated rate. The horizontal dashed line gives the SK-IV total average (0.451). Error bars shown are statistical plus energy-uncorrelated systematic uncertainties. Right: SK-I+II+III+IV recoil electron spectrum compared to the no-oscillation expectation. The green (blue) shape is the MSW expectation using the SK (solar+KamLAND) best-fit oscillation parameters. The orange (black) line is the best-fit to SK data with a general exponential/quadratic (cubic) $P_{ee}$ survival probability.

background components, with the fraction of events in each sub-sample determined by MC simulated events. The right panel of Fig. 1 shows the measured angular distributions and fit results for the energy ranges of 3.5-4.0 MeV, 4.0-4.5 MeV, 4.5-5.0 MeV and 7.0-7.5 MeV. As expected in the lowest energy bins, the background component is the largest in the sub-samples with the lowest MSG, while the signal component grows as the MSG is increased. Using this method of MSG sub-samples has reduced the total uncertainty by up to 15% for the lowest energy bins. The left panel of Fig. 2 shows the resulting SK-IV recoil electron energy spectrum, where below 7.5 MeV sub-samples of MSG has been used and above 7.5 MeV the standard signal extraction method is used.

*5.2.2. SK Combined Solar Neutrino Energy Spectrum Analysis*

The spectral data from SK-III has been refit using the same energy bins and MSG sub-samples as SK-IV, down to 4.0 MeV. The gain in precision in SK-III is similar as to SK-IV. However, in SK-II, the same MSG sub-sample have been applied for all energy bins. In order to discuss the energy dependence of the solar neutrino flavor composition in a general way, the electron neutrino survival probability $P_{ee}$ has been parameterized using a general quadratic function $P_{ee} = c_0 + c_1(E_\nu - 10) + c_2(E_\nu - 10)^2$, as SNO did in [14], and then by general exponential and cubic functions as well. Each phase of SK is fit separately, and then combined together using a minimum chi-squared method. The right panel of Fig. 2 shows the statistical combination of the four phases of SK, along with the best-fits coming from the general quadratic/exponential (identical and shown in orange) and general cubic (black) function fits. Also shown in green (blue) is the expected MSW resonance curves assuming the best-fit neutrino oscillation parameters coming from a fit to SK data only (all solar neutrino plus KamLAND [4] data). This figure is shown only as an illustration of the resulting SK combine fit and should not be used to do further analysis. Fig. 3 shows the resulting $1\sigma$ uncertainties on the spectrum fit to the general functions, along with the expected MSW curves (same as in Fig. 2).

There are added benefits when combining the results of the quadratic fit to the survival probability of SK and SNO together, since SK's correlation between the quadratic coefficients $c_1$ and $c_2$ is opposite to that of SNO's. The resulting combine $c_1 - c_2$ correlation becomes much smaller. The addition of the SK data to the SNO data not only significantly increases the precision of the $c_0$ determination, but the uncertainties on the shape are reduced. While SK data by itself prefers an "upturn" when going from high to low neutrino energy and SNO data prefers a "downturn", the combined fit favors an "upturn" more strongly than the SK data by itself. SNO's sensitivity is dominated by charged-current interactions which preserve the neutrino energy, however, the nuclear threshold energy takes away

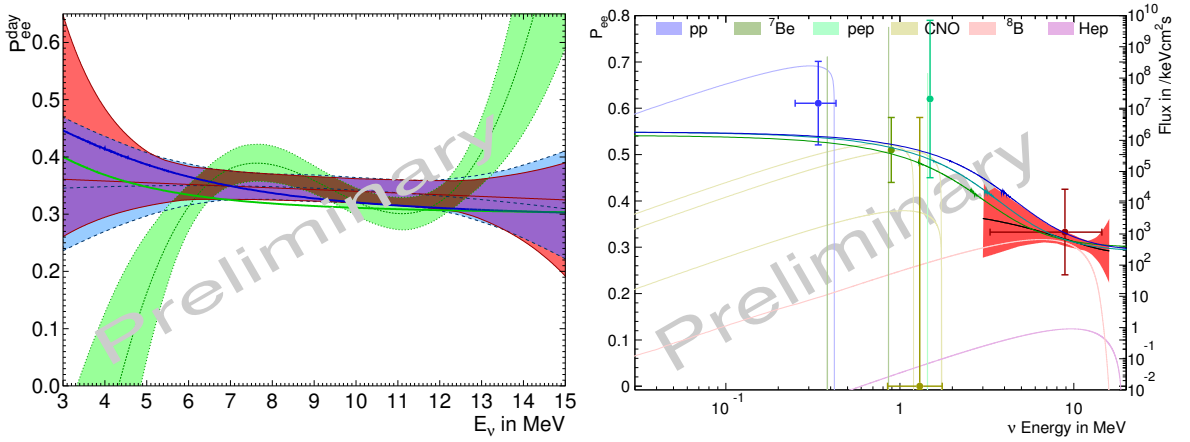


Figure 3: Left: Allowed survival probability $1\sigma$ band from SK data. The red (blue) area is based on an exponential (quadratic) fit and the green band is based on a cubic fit. The $^8$B flux is constrained to the measurement from SNO. The absolute value of the $^8$B flux doesn't affect the shape constraint much, just the average value. Also shown are predictions based on the oscillation parameters of a fit to all solar data (green) and a fit to all solar+KamLAND data (blue). Right: Predicted solar neutrino spectra [16]. Overlaid are expected MSW survival probabilities; green is the expectation assuming oscillation parameters from the SK best-fit, turquoise from the global solar neutrino best-fit and blue from the solar plus KamLAND best fit. The $1\sigma$ band from the combined data of SK and SNO is shown in red. Also shown are measurements of the $^7$Be (green point), *pep* (light green point) and $^8$B flux (red point) by Borexino [18], as well as *pp* (blue point) and CNO values (gold point) extracted from other experiments [17].

some of the advantage over SK, which has higher statistics in the elastic scattering data. As a consequence, SNO's uncertainties are smaller at higher neutrino energy, while SK's uncertainties are smaller at lower neutrino energy. The right panel of Fig. 3 superimposes the SK plus SNO $1\sigma$ $P_{ee}$ quadratic fit band (red) (on a logarithmic scale) on the SSM [16] solar neutrino spectrum. Also shown are the *pp* and CNO neutrino flux constraints from all solar neutrino data [3, 17] and the $^7$Be, *pep* and $^8$B flux measurements of the Borexino experiment [18]. The SK and SNO combined allowed band (and the other solar data) are in good agreement with the predicted MSW curves based on either SK data only, all solar neutrino data or all solar neutrino plus KamLAND data (shown in green, turquoise and blue, respectively).

### *5.3. Solar Neutrino Day-Night Flux Asymmetry*

The matter density of the Earth affects solar neutrino oscillations while the Sun is below the horizon. This so called "day-night effect" will lead to an enhancement of the $\nu_e$ flavor content during the nighttime for most oscillation parameters. The most straight-forward test of this effect uses the solar zenith angle $\theta_z$ at the time of each event to separately measure the solar neutrino flux during the day $\Phi_D$ (defined as $\cos\theta_z \leq 0$) and the night $\Phi_N$ (defined as $\cos\theta_z > 0$). The day-night asymmetry $A_{DN} = (\Phi_D - \Phi_N)/\frac{1}{2}(\Phi_D + \Phi_N)$ defines a convenient measure of the size of the effect.

The SK-IV livetime during the day (night) is 626.4 days (679.9 days). The solar neutrino flux between 4.5 and 19.5 MeV and assuming no oscillations is measured as $\phi_D = [2.29 \pm 0.03(\text{stat.}) \pm 0.05(\text{sys.})] \times 10^6$ /(cm$^2$sec) during the day and $\phi_N = [2.42 \pm 0.03(\text{stat.}) \pm 0.05(\text{sys.})] \times 10^6$ /(cm$^2$sec) during the night. By comparing the separately measured day and night fluxes, the measured day-night asymmetry for SK-IV is found to be $[-5.3 \pm 2.0(\text{stat.}) \pm 1.4(\text{sys.})]\%$. When this is combined with the previous three phases (see the center column of Table 2), SK measures the day-night asymmetry in this simple way as $[-4.2 \pm 1.2(\text{stat.}) \pm 0.8(\text{sys.})]\%$ [7]. This result deviates from zero by $2.8\sigma$.

To eliminate systematic effects and increase statistical precision, a more sophisticated method to test the day-night effect is given in [19, 1]. For a given set of oscillation parameters, the interaction rate as a function of the solar zenith angle is predicted. Only the shape of the calculated solar zenith angle variation is used, the amplitude of it is scaled

Table 2: Day-night asymmetry for each SK phase, coming from separate day and night rate measurements (middle column) and the amplitude fit (right column). The uncertainties shown are statistical and systematic. The entire right column assumes the SK best-fit point of oscillation parameters.

| | $A_{\mathrm{DN}} \pm (\mathrm{stat}) \pm (\mathrm{syst})$ | $A_{\mathrm{DN}}^{\mathrm{fit}} \pm (\mathrm{stat}) \pm (\mathrm{syst})$ |
|---|---|---|
| SK-I | $(-2.1 \pm 2.0 \pm 1.3)\%$ | $(-2.0 \pm 1.7 \pm 1.0)\%$ |
| SK-II | $(-5.5 \pm 4.2 \pm 3.7)\%$ | $(-4.3 \pm 3.8 \pm 1.0)\%$ |
| SK-III | $(-5.9 \pm 3.2 \pm 1.3)\%$ | $(-4.3 \pm 2.7 \pm 0.7)\%$ |
| SK-IV | $(-5.3 \pm 2.0 \pm 1.4)\%$ | $(-3.4 \pm 1.8 \pm 0.6)\%$ |
| Combined | $(-4.2 \pm 1.2 \pm 0.8)\%$ | $(-3.2 \pm 1.1 \pm 0.5)\%$ |

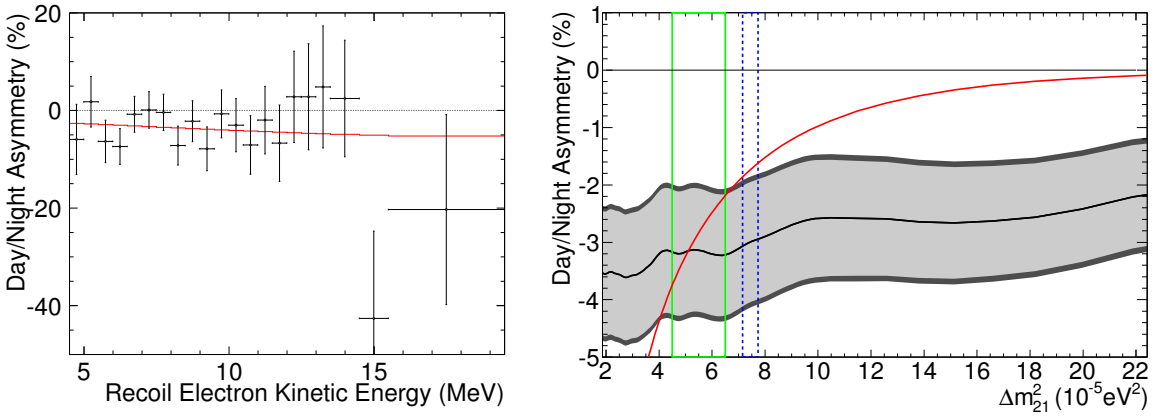


Figure 4: Left: SK day-night amplitude fit as a function of recoil electron kinetic energy, shown as the measured amplitude times the expected day-night asymmetry, for oscillation parameters chosen by the SK best-fit. The error bars shown are statistical uncertainties only and the expected dependence is shown in red. Right: Dependence of the measured day-night asymmetry (fitted day-night amplitude times the expected day-night asymmetry (red)) on $\Delta m^2_{21}$, for $\sin^2\theta_{12} = 0.314$ and $\sin^2\theta_{13} = 0.025$. The $1\sigma$ stat (stat+syst) uncertainties are given by the light (dark) gray band. Overlaid are the $1\sigma$ allowed ranges from the solar global fit (green box) and the KamLAND experiment (blue box).

by an arbitrary parameter. The extended maximum likelihood fit to extract the solar neutrino signal is expanded to allow time-varying signals. The likelihood is then evaluated as a function of the average signal rates, the background rates and a scaling parameter, termed the "day-night amplitude". The equivalent day-night asymmetry is calculated by multiplying the fit scaling parameter with the expected day-night asymmetry. In this manner the day-night asymmetry is measured more precisely statistically and is less vulnerable to some key systematic effects.

Because the amplitude fit depends on the assumed shape of the day-night variation (given for each energy bin in [19] and [1]), it necessarily depends on the oscillation parameters, although with very little dependence expected on the mixing angles (in or near the large mixing angle solution and for $\theta_{13}$ values consistent with reactor neutrino measurements [20]). The fit is run for parameters covering the MSW region of oscillation parameters ($10^{-9}$ eV$^2 \leq \Delta m^2_{21} \leq 10^{-3}$ eV$^2$ and $10^{-4} \leq \sin^2\theta_{12} < 1$), for values of $\sin^2\theta_{13}$ between 0.015 and 0.035. Details of the estimates of the systematic uncertainties resulting from this method are given in [6].

The resulting day-night asymmetry when using the extended maximum likelihood method can be seen for individual phases in the right column of Table 2. The left panel of Fig. 4 shows the combined SK-I+II+III+IV day-night amplitude fit as a function of recoil electron energy. In each recoil electron energy bin $e$, the day-night variation is fit to an amplitude $\alpha_e$. The displayed day-night asymmetry values are the product of the fit amplitude $\alpha_e$ with the expected day-night asymmetry $A^e_{\mathrm{DN,\,calc}}$ (red), when using the SK best-fit point of oscillation parameters ($\Delta m^2_{21} = 4.84 \times 10^{-5}$ eV$^2$, $\sin^2\theta_{12} = 0.342$ and $\sin^2\theta_{13} = 0.025$). These parameters are chosen when using SK's spectral and time variation

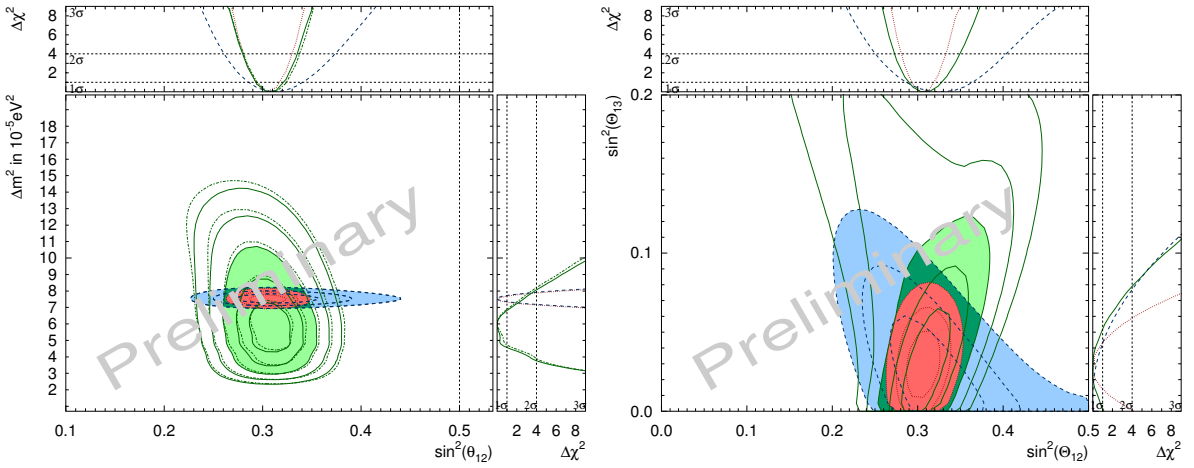


Figure 5: Left: Allowed contours of $\Delta m^2_{21}$ vs. $\sin^2\theta_{12}$ from solar neutrino data (green) at 1, 2, 3, 4 and 5$\sigma$ and KamLAND data (blue) at the 1, 2 and 3$\sigma$ confidence levels. Also shown is the combined result in red. For comparison, the almost identical result of the SK+SNO combined fit is shown by the dashed dotted lines. The filled regions give the 3$\sigma$ confidence levels. $\theta_{13}$ is constrained by $\left(\frac{\sin^2\theta_{13}-0.0242}{0.0026}\right)^2$. Right: Allowed contours of $\sin^2\theta_{13}$ vs. $\sin^2\theta_{12}$, colors are the same as the left panel.

data along with constraints on the $^8$B solar neutrino flux and $\theta_{13}$. When all energy bins are fit together and the same oscillation parameters assumed, the resulting SK-measured day-night asymmetry coming from the amplitude fit is

$$A_{\rm DN}^{\rm fit} = [-3.2 \pm 1.1(\text{stat.}) \pm 0.5(\text{sys.})]\% \text{ [7]},$$

with an asymmetry of −3.3% expected by numerical calculations (see [19] for details). This result deviates from zero by 2.7$\sigma$, giving the first significant direct indication for matter enhanced neutrino oscillations.

If this value is combined with SNO's measurement [14], the resulting measured SK equivalent day-night asymmetry is $A_{\rm DN}^{\rm fit} = [-2.9 \pm 1.0(\text{stat.+sys.})]\%$, increasing the significance for a non-zero day-night asymmetry to 2.9$\sigma$. While the expected day-night asymmetry at SK changes to −1.7% if the value of $\Delta m^2_{21}$ is changed to $7.41 \times 10^{-5}$ eV$^2$ (motivated by KamLAND data [4]), the measured value is found to be $A_{\rm DN}^{\rm fit} = [-3.0 \pm 1.0(\text{stat.}) \pm 0.5(\text{sys.})]\%$, reducing the significance for a non-zero day-night asymmetry from 2.7 to 2.6$\sigma$. The dependence of the SK measured day-night asymmetry on $\Delta m^2_{21}$, for $\sin^2\theta_{12} = 0.314$ and $\sin^2\theta_{13} = 0.025$, can be seen in the right panel of Fig. 4, with the expected day-night asymmetry shown by the red curve. Superimposed are the 1$\sigma$ allowed ranges in $\Delta m^2_{21}$ from the solar global fit [6] (green) and from the KamLAND experiment [4]. The resulting day-night asymmetry has negligible dependence on the values of $\theta_{12}$ (within the LMA region) and $\theta_{13}$ (near the reactor antineutrino best-fit [20]).

### *5.4. Solar Neutrino Oscillation Analysis*

We analyzed the SK-IV elastic scattering rate, the recoil electron spectral shape and the day-night variation to constrain the solar neutrino oscillation parameters. We then combined the SK-IV constraints with those of the previous three SK phases, as well as all other solar neutrino experiments. The allowed contours of all solar neutrino data (as well as KamLAND's constraints) are shown in Fig. 5. SK and SNO dominate the combined fit to all solar neutrino data. This can be seen from the almost identical two sets of green contours in the left panel of Fig. 5. In the side panel of this figure, some tension between the solar neutrino and reactor antineutrino measurements of the solar $\Delta m^2_{21}$ is evident, stemming from the SK day-night measurement. Even though the expected amplitude agrees within $\sim 1.1\sigma$ with the fitted amplitude for any $\Delta m^2_{21}$, in either the KamLAND or the SK range, the SK data somewhat favor the shape of the variation predicted by values of $\Delta m^2_{21}$ that are smaller than KamLAND's. The right panel of Fig. 5 shows the results of the $\theta_{13}$ unconstrained fit. The significance of non-zero $\theta_{13}$ from the solar+KamLAND data combined fit is about 2$\sigma$, measured as $\sin^2\theta_{13} = 0.026^{+0.017}_{-0.012}$ and quite consistent with reactor antineutrino measurements [20].

## 6. Conclusion

The fourth phase of SK measured the solar $^8$B neutrino-electron elastic scattering-rate with the highest precision yet. When combined with the results from the previous three phases, the SK combined flux is $[2.37 \pm 0.015(\text{stat}) \pm 0.04(\text{syst})] \times 10^6$ /(cm$^2$sec). A quadratic fit of the electron-flavor survival probability as a function of energy to all SK data, as well as a combined fit with SNO solar neutrino data, slightly favors the presence of the MSW resonance. The solar neutrino elastic scattering day-night rate asymmetry is measured as $[-3.2 \pm 1.1(\text{stat}) \pm 0.5(\text{syst})]\%$. This solar zenith angle variation data gives the first significant indication for matter enhanced neutrino oscillation, and leads SK to having the world's most precise measurement of $\Delta m^2_{21} = 4.8^{+1.8}_{-0.9}$ eV$^2$, using neutrinos rather than anti-neutrinos. There is a slight tension of $1.5\sigma$ between this value and KamLAND's measurement using reactor anti-neutrinos. The tension increases to $1.6\sigma$, if other solar neutrino data are included. A $\theta_{13}$ constrained fit to all solar neutrino data and KamLAND yields $\sin^2\theta_{12} = 0.305 \pm 0.013$ and $\Delta m^2_{21} = 7.49^{+0.19}_{-0.17} \times 10^{-5}$ eV$^2$. When this constraint is removed, solar neutrino experiments and KamLAND measure $\sin^2\theta_{13} = 0.026^{+0.017}_{-0.012}$, a value in good agreement with reactor antineutrino measurements.

## References


[1] J. Hosaka *et al.*, Phys. Rev. D **73**, 112001 (2006).
[2] Q. R. Ahmad, Phys. Rev. Lett. **87**, 071301 (2001).
[3] R. Davis, Jr. ,D. S. Harmer, and K. C. Hoffman *et al.*, Phys. Rev. Lett. **20**, 1205 (1968).
[4] S. Abe *et al.*, Phys. Rev. Lett. **100**, 221803 (2008);
The KamLAND Collaboration, arxiv:1303.4667v2 (2013).
[5] S. P. Mikheyev and A. Y. Smirnov, Sov. Jour. Nucl. Phys. **42**, 913 (1985);
L. Wolfenstein, Phys. Rev. D **17**, 2369 (1978).
[6] A. Renshaw, Ph.D. Thesis, University of California-Irvine 2013, http://www-sk.icrr.u-tokyo.ac.jp/sk/pub/Renshaw_Doctoral_Thesis.pdf;
K. Abe *et al.*, (to be published).
[7] A. Renshaw *et al.*, Phys. Rev. Lett. **112**, 091805 (2014).
[8] K. Abe *et al.*, Phys. Rev. D **83**, 052010 (2011).
[9] H. Nishino *et al.*, Nucl. Inst. and Meth. A **620** (2009).
[10] K. Abe *et al.*, Nucl. Inst. and Meth. A **737** (2014).
[11] M. Nakahata *et al.*, Nucl. Instr. and Meth. A **421**, 113 (1999).
[12] E. Blaufuss *et al.*, Nucl. Instr. and Meth. A **458**, 636 (2001).
[13] J. P. Cravens *et al.*, Phys. Rev. D **78**, 032002 (2008).
[14] B. Aharmin *et al.*, Phys. Rev. C **88**, 025501 (2013).
[15] B. Aharmin *et al.*, Astrophys. J. **653**, 1545 (2006).
[16] J. N. Bahcall, A. M. Serenelli, and S. Basu, Astrophys. J. Suppl. **165**, 400 (2006).
[17] J. N. Abdurashitov *et al.* (SAGE collaboration), Phys. Rev. C **80**, 015807 (2009);
M. Altmann *et al.* (GALLEX Collaboration), Phys. Lett. B **616**, 174 (2005);
G. Bellini *et al.* (Borexino Collaboration), Phys. Rev. Lett. **107**, 141302 (2011).
[18] Bellini *et al.* (Borexino Collaboration), Phys. Rev. D **82**, 033006 (2010); Bellini *et al.* (Borexino Collaboration), Phys. Rev. Lett. **707**, 051302 (2012).
[19] M. B. Smy *et al.*, Phys. Rev. D**69**, 011104(R) (2004).
[20] F. P. An *et al.* (Daya Bay Collaboration), Chin. Phys. C**37**, 011001 (2013); J. K. Ahn *et al.* (RENO Collaboration), Phys.Rev.Lett. **108**, 191802 (2012); Y. Abe *et al.* (Double Chooz Collaboration), Phys.Rev. D**86**, 052008 (2012); J. Beringer *et al.* (Particle Data Group), Phys. Rev. D**86**, 010001 (2012).